

A computational study of direct CO₂ hydrogenation to methanol on Pd surfaces

Igor Kowalec ^a, Lara Kabalan ^a, C. Richard A. Catlow ^{a,b,c} and Andrew J. Logsdail ^{a,*}

^a Cardiff Catalysis Institute, School of Chemistry, Cardiff University, Cardiff, United Kingdom

^b UK Catalysis Hub, Research Complex at Harwell, RAL, Oxford, OX11 0FA, United Kingdom

^c Department of Chemistry, University College London, London, WC1H 0AJ, United Kingdom

* Email: LogsdailA@cardiff.ac.uk

Abstract

The reaction mechanism of direct CO₂ hydrogenation to methanol is investigated on Pd (111), (100) and (110) surfaces using density functional theory (DFT), providing detailed insight into the reactivity of CO₂ on these Pd-based catalysts. Hydrogen adsorption is first considered on the surfaces of interest, with high-coordination sites having the largest adsorption energy and being connected by diffusion channels with low energy barriers. The chemisorption of CO₂ to the surfaces, forming a partially charged CO₂^{δ-}, is weakly endothermic on a Pd (111), with an adsorption energy of 0.06 eV, and slightly exothermic on Pd (100) and (110), with adsorption energies of -0.13 and -0.23 eV, respectively. The low stability of CO₂^{δ-} on the Pd (111) surface is attributed to negative charge accumulation on the surface Pd atoms interacting directly with the CO₂^{δ-} adsorbate, identified via Mulliken analysis. Detailed consideration for hydrogenation of the adsorbed species on the Pd surface shows that HCOOH hydrogenation to H₂COOH would be the rate determining step of the conversion to methanol in all cases, with activation barriers of 1.35, 1.26, and 0.92 eV on Pd (111), (100) and (110) surfaces, respectively. We show that Pd (100) and (110) surfaces exhibit overall lower activation energies than the most studied Pd (111) surface and should be investigated in future Pd catalytic studies.

1. Introduction

Methanol synthesis by direct hydrogenation of CO₂ has been recognised as a potential route towards sustainable fuels for transport and a circular fuel economy.¹ The industrial synthesis of methanol involves syngas, which is a mixture of CO/CO₂/H₂ produced from coal gasification. Whilst methanol synthesis from fossil fuels is efficient and profitable, environmental pressures are urging the chemical industry to transfer from a linear-oil economy to net zero emissions by 2050.² Bussche *et al.* built a steady-state kinetic model that revealed CO₂, and not CO, is likely to be the main source of carbon in methanol synthesised from syngas;^{2,3} such knowledge allows consideration of direct CO₂ hydrogenation to methanol, using anthropogenic CO₂ from the atmosphere. However, a better understanding of the CO₂ interaction with transition metal catalysts is required for the design of novel and effective catalytic systems. Many factors, such as the source of H₂, affect the extent to which the process of direct methanol synthesis from CO₂ can be “green”; however, the idea of using of an atmospheric pollutant such as CO₂ for fuel synthesis, and/or also generating feedstock for further synthesis of chemical compounds, such as formic acid, is broadly appealing.⁴

A crucial step in the direct hydrogenation of CO₂ to methanol is the initial CO₂ activation. On a heterogeneous catalyst, the reverse water-gas shift (RWGS) reaction needs to be inhibited while maintaining a strong interaction between CO₂ and the catalytic surface.^{4,5} Pd alone exhibits poor selectivity to methanol for direct CO₂ hydrogenation, but the selectivity is greatly enhanced when it is alloyed with other transition metals, such as Zn.^{4,6–10} In order to understand fully the Pd-based alloy reactivity, it is necessary first to know the nature of interactions between CO₂ and Pd. The available experimental data for the interaction of CO₂ with Pd facets is limited, but computation using density functional theory (DFT) is providing insight into the processes.^{11–14} Burghaus *et al.* reported that CO₂ reactivity on clean Pd surfaces is weak, not favouring dissociation to CO unless an alkali metal species is coadsorbed.¹⁴ The weak interaction is considered to be predominantly a Van der Waals physisorption, based on the theoretical and experimental observations at the Pd (111) surface.^{13,15,16} CO₂ adsorption on Pd has been studied in the context of RWGS reaction and utilisation of syngas, and desorption of CO₂ from the Pd (111) surface reported as requiring 0.26 eV of energy.¹³ Solymosi *et al.* reported that CO₂ desorption from the Pd (100) surface also has a relatively low energy, 0.35 eV; this was, however, associated with a chemisorption, involving a metal to empty CO₂ π* orbital electron transfer.¹¹ Evidence of CO₂ chemisorption Pd (110) in the presence of water was also reported by Brosseau *et al.*¹⁷ Therefore, the character of the CO₂ interaction with Pd surfaces seems to depend on the particular surface structure. The differing adsorption energies can be correlated with surface energies, given physisorption was exclusively observed on the lowest energy (111) surface, and

experimental evidence of chemisorption was observed for CO₂ on the higher energy Pd (100) and (110) surfaces, though the latter is noted as being in the presence of water.^{11–13,17}

Complementary to these observations, the rate for catalytic hydrogenation of CO₂ on Pd is reported as greatly increased when the active species is paired with suitable metal oxide supports, such as TiO₂ and ZnO, as they facilitate CO₂ adsorption and activation.^{8,18,19} Ko *et al.* computed the adsorption of CO₂ on transition metal surfaces, using the dispersion-corrected PBE-D2 density functional, and reported two types of CO₂ adsorption on Pd (111): an exothermic physisorption (-0.33 eV) of undistorted CO₂, parallel to the surface; and a less exothermic chemisorption (-0.18 eV) with CO₂ in a bent geometry, and having a partial negative charge.²⁰ In contrast, Zhang *et al.* recently calculated the CO₂ chemisorption on Pd (111) to be endothermic (0.06 eV) using the PBE density functional, in agreement with Habas *et al.*, who reported the adsorption energy of CO₂ to be 0.22 eV above the dissociation limit using DFT with the B3LYP density functional.²¹ Liu *et al.* have also shown that, when using the PBE density functional, the inclusion of the DFT-D2 correction dramatically changes the adsorption energy of chemisorbed species on the Pd (111) surface, from 0.30 eV to -0.18 eV.¹⁶ Although there is no consensus on the matter of CO₂ chemisorption endo- or exothermicity on Pd surfaces, the reported values are generally small, which agrees with the experimental reports of weak interaction between CO₂ and Pd surfaces.

Direct CO₂ hydrogenation to methanol is proposed to proceed via a surface formate intermediate (HCOO*, where * indicates an adsorbed species), with Medford *et al.* having shown that HCOO* could act as a poison for other reaction pathways due to its high thermodynamic stability on the catalyst surface.²² Variations of the mechanism proposed by Grabow, which progresses via formic acid (HCOOH) as shown in Figure 1, have been presented, such as an initial Eley-Rideal type mechanism on Cu-based catalytic systems, where CO₂ in the gas phase reacts with surface-bound hydrogen to yield formate.²³ Recently, Huš *et al.* concluded that dioxymethylene (H₂CO₂*) should be preferably considered over formic acid (HCOOH*) on Cu-based catalysts as the former is more strongly bound to the metallic surface and the activation energy towards hydroxymethoxy (H₂COOH*) is lower.²⁴

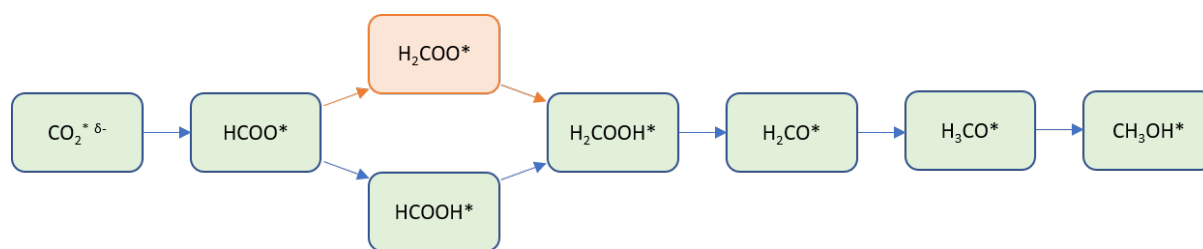


Figure 1. Formate pathway of direct CO₂ hydrogenation to methanol on metallic surfaces, as proposed by Grabow *et al.* (via HCOO*, blue) and Huš *et al.* (via H₂COO*, orange). * indicates a surface-bound species and δ- indicates that CO₂ is partially charged (i.e. activated).^{24,25}

Pd-based catalysts supported on ZnO are potent alternative catalysts for this reaction, with their reactivity attributed to the Pd-Zn binary metallic phases and their stabilisation of the HCOO* intermediate, similar to the Cu-based catalyst.^{8,19} Zhang *et al.* have reported DFT studies of an alternative CO₂ formate mechanism that involves dissociation of HCOOH to HCO and OH, and subsequent hydrogenations of HCO to produce CH₃OH.²⁶ On the other hand, Brix *et al.* have recently considered the initial CO₂ hydrogenation on Pd (111) to proceed via carboxylic acid (COOH), instead of formate, in their DFT study using the dispersion-corrected PBE-D3 density functional, and they observed a high energy barrier of 2.23 eV for CO₂ hydrogenation to formate on Pd (111), in contrast to the barrier of 0.85 eV reported by Zhang *et al.*^{23,24}

Whilst binary metallic alloy catalysts may offer better selectivity, stability and tunability than their monometallic counterparts, a basic understanding of the behaviour of monometallic materials is essential to design these new multi-component materials. To achieve this insight in the context of CO₂ hydrogenation over Pd, one needs to understand reactivity across all of the prominent surface facets. Thus, we present here an in-depth investigation of CO₂ interaction with low energy Pd (111), (110) and (100) surfaces using DFT calculations, followed by investigation of the direct CO₂ hydrogenation to CH₃OH, *via* the Grabow mechanism, on the Pd (111), (110) and (100) surfaces, in the context of rationalising CO₂ reactivity on Pd-based catalysts.

2. Methodology

The Fritz Haber Institute *ab initio* molecular simulations (FHI-aims) software package has been used for full potential all-electron DFT calculations, with the Pythonic Atomic Simulation Environment (ASE) used for management of calculation geometries.^{27,28} The default convergence criteria within FHI-aims for self-consistent field (SCF) calculations were used, i.e. the changes between the current and previous SCF iterations in charge density, sum of eigenvalues and total energy were below $N \times 1.67 \times 10^{-5} e a_0^{-3}$, 10^{-3} eV and 10^{-6} eV, respectively, where N is the number of atoms in the model. Scalar relativistic treatment of kinetic energy for all elements was achieved by the atomic zero-order regular approximation (ZORA), and a Gaussian-type broadening with width of 0.01 eV was applied to the occupation of electronic states. The Perdew-Burke-Ernzerhof exchange correlation (XC) density functional has been unless explicitly stated otherwise, paired with the Tkatchenko-Scheffler Van der Waals dispersion correction (PBE+vdW). A default “light” basis set has been used for geometry optimisations, providing structural accuracy;^{27,29,30} energy calculations were then performed with a “tight” basis set on the optimised geometries, providing greater electronic accuracy and mitigation of basis set superposition error.²⁷ For geometry optimisations, convergence was deemed complete when forces on all unconstrained atoms were less than 0.01 eV/Å.

Due to the closed-shell electronic configuration of Pd ([Kr] 4d¹⁰), spin-paired calculations were used in periodic calculations; gas-phase adsorbate structures were calculated both spin-paired and spin-unpaired, and the energy of the more stable system was considered for reference to periodic calculations. The effect of the spin-paired approximation has been assessed towards the activation energies in relevant surface hydrogenation reactions in Section S3 of the Supporting Information (SI), with a spin-paired treatment shown to introduce small error bars of ± 0.05 eV.

2.1 Bulk models

For sampling the Brillouin zone of face-centred cubic (FCC) Pd in a primitive unit cell, a $(9 \times 9 \times 9)$ Monkhorst–Pack \mathbf{k} -grid provides converged accuracy, as detailed in Section S1 of the SI.³¹ The lattice constant ($a_0 = 3.914$ Å), bulk modulus ($B_0 = 183.37$ GPa) and cohesive energy ($E_{coh} = 3.996$ eV) calculated for bulk FCC Pd match closely with the experimental observations of 3.88 Å, 180.40 GPa and 3.89 eV, respectively.^{32,33}

2.2 Surface models

Using the optimised model of bulk FCC Pd, a surface supercell was created with dimensions of $(3 \times 3 \times n)$, where n is the number of atomic layers in the z -direction perpendicular to the material surface. The x - and y -dimensions were chosen such that the adsorbates are significantly separated (7.5 \AA), and a vacuum layer of 40 \AA was added in the z -direction. The k -grid sampling was reduced appropriately for altered cell dimensions, with a k -grid of $(3 \times 3 \times 1)$ applied. Due to the one-sided nature of the slab models considered, a dipole-correction was used in all calculations.

The energy penalty for breaking chemical bonds at the surface of a material (E_{cleave}) is calculated as:

$$E_{\text{cleave}} = \frac{E_{\text{Slab}}^{\text{Unrelaxed}} - N \cdot E_{\text{bulk}}}{2A} \quad \text{Equation 1.}$$

where the DFT total energy of a surface slab model ($E_{\text{Slab}}^{\text{Unrelaxed}}$), the bulk energy per atom (E_{bulk}), the number of atoms in the model (N), and the surface area (A), are necessary. E_{cleave} converges for the Pd (111), (100) and (110) facets when $n \geq 5$, as shown in Figure 2, and 5 layer models are used for all subsequent calculations.

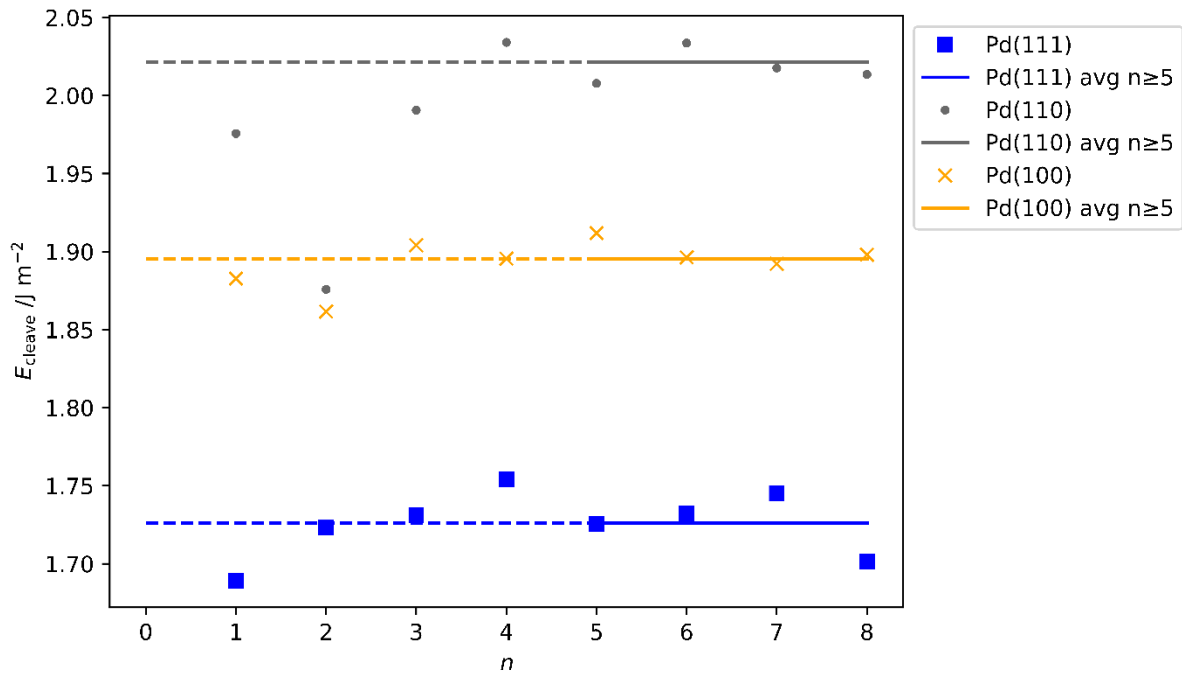


Figure 2. E_{cleave} calculated for Pd FCC (111), (110) and (100) surfaces as a function of increasing model thickness, n . A key is provided to identify the symbols and linear fits; the average cleave energy (solid horizontal line) was taken from $n \geq 5$, to avoid bias from inaccurate thin slabs (dashed lines).

To calculate the surface energy (E_{surf}), the energy of stabilisation provided by geometry relaxation (E_{relax}) needs to be obtained from the difference in total DFT energy of the optimised slab ($E_{\text{Slab}}^{\text{Relaxed}}$) and $E_{\text{Slab}}^{\text{Unrelaxed}}$:

$$E_{\text{relax}} = \frac{E_{\text{Slab}}^{\text{Relaxed}} - E_{\text{Slab}}^{\text{Unrelaxed}}}{A} \quad \text{Equation 2.}$$

where a single-sided model of the surface is considered, hence the denominator is A only. Constraints were used to maintain the bulk structure for Pd atoms distant from the adsorption site, i.e. the bottom layers of the slab model. $E_{\text{Slab}}^{\text{Relaxed}}$ was calculated for all three surface facets with one, two or three layers of surface atoms unconstrained, with E_{relax} converging only when the top three surface layers are unconstrained.

In summary, a $3 \times 3 \times 5$ supercell surface model has been with the bottom two layers constrained to their bulk positions, and the three top surface layers unconstrained, has been identified as accurate for our surface model. The surface energies (E_{surf}) can then be calculated as follows:

$$E_{\text{surf}} = E_{\text{cleave}} + E_{\text{relax}} \quad \text{Equation 3.}$$

with these settings, and is presented in Table 1. The calculated Pd (111), (100) and (110) E_{surf} match previous computation and experiments, thus supporting the validity of our approach.

Table 1. Pd FCC (111), (100) and (110) surface energies calculated using the outlined settings. Literature and experiment are provided for comparison.

Ref	XC	$E_{\text{surf}} / (\text{J m}^{-2})$		
		Pd (111)	Pd (100)	Pd (110)
This work	PBE+vdW	1.72	1.91	1.99
Methfessel <i>et al.</i> ³⁴	LDA	1.64	1.86	1.97
Vitos <i>et al.</i> ³⁵	GGA	1.92	2.33	2.23
Patra <i>et al.</i> ³⁶	LDA	1.88	2.43	2.25
	PBE	1.36	1.79	1.61
	PBEsol	1.63	2.15	1.93
	SCAN	1.54	2.03	1.83
	SCAN+rVV10	1.77	2.29	2.05
Singh-Miller <i>et al.</i> ³⁷	PBE	1.31	1.49	1.55
Da Silva <i>et al.</i> ³⁸	LDA	1.87	-	-
	PBE	1.33	-	-
Skriver <i>et al.</i> ³⁹	LDA	1.88	-	-
Tyson <i>et al.</i> ⁴⁰	Experiment	2.00	-	-
Boer <i>et al.</i> ⁴¹	Experiment	2.01	-	-

2.3 Surface adsorption

For surface reactions, the adsorption energy (E_{ads}) measures the interaction between a catalyst and reactant, and is deduced from comparison of the energies of the optimised gas-phase adsorbate (E_A), optimised surface (E_S) and the combined system (E_{A-S}).

$$E_{\text{ads}} = E_{A-S} - (E_A + E_S) \quad \text{Equation 4.}$$

where a negative value indicates favourable adsorption. Due to basis set incompleteness when using an atom centred basis, a Boys-Bernardi counterpoise correction is necessary for surface-adsorbate interactions to account for the basis set superposition error (BSSE).⁴² In our work, the BSSE for CO₂ adsorbed on Pd (111) was assessed on an aperiodic model with all Pd atoms within 7.0 Å of the adsorbed CO₂ molecule included (i.e. all atoms within the basis set cutoff, including those in neighbour cells). The energy of the CO₂ in the presence and absence of Pd basis functions ($E_{A(A-S)}$ and $E_{A(A)}$, respectively) were compared, and the equivalent comparison of the energy of the slab model in the presence and absence of the basis functions of the CO₂ adsorbate ($E_{S(A-S)}$ and $E_{S(S)}$, respectively) was also performed.⁴² The BSSE energy (E_{BSSE}) was then calculated as:⁴²

$$E_{\text{BSSE}} = [E_{A(A-S)} - E_{A(A)}] + [E_{S(A-S)} - E_{S(S)}] \quad \text{Equation 5.}$$

The more negative the E_{BSSE} , the higher the overbinding error. By subtracting E_{BSSE} from E_{ads} , the counterpoise corrected adsorption energy can be established ($E_{\text{ads}}^{\text{CP}}$) as:

$$E_{\text{ads}}^{\text{CP}} = E_{\text{ads}} - E_{\text{BSSE}} \quad \text{Equation 6.}$$

With the “light” basis set, E_{BSSE} is -0.08 eV for CO₂ on Pd (111), but E_{BSSE} was reduced to -0.02 eV with the “tight” basis set. Considering the low BSSE with the “tight” basis, which is used subsequently throughout this work, the E_{BSSE} contribution to E_{ads} was deemed negligible and was not calculated for species other than CO₂.

2.4 Transition state structures

For kinetic studies, we have used a machine learning nudged elastic band (MLNEB) method to identify saddle points and minimum energy paths (MEPs).^{43,44} A spring constant of 0.05 eV/Å has been used throughout; the convergence criterion of forces on all unconstrained atoms of below 0.05 eV/Å, with energy uncertainty below 0.03 eV, was deemed sufficiently accurate for CO₂ adsorption. Comparison with a more stringent force criterion of 0.01 eV/Å altered the activation energy for CO₂ adsorption on FCC (111) surface by 5 meV only (Section S2, SI).

3. Results and discussions

3.1 Hydrogen adsorption

Prior to investigating the reaction steps in CO₂ hydrogenation, it is crucial to gain an understanding of hydrogen behaviour on Pd. Thus, a survey was conducted of E_{ads} for H, $E_{\text{ads}}(\text{H})$, on the Pd surfaces; the H atom was positioned at various locations on the surface and optimised, with constraints in the xy -plane. $E_{\text{ads}}(\text{H})$ on the Pd (111), (100), and (110) surfaces, calculated with respect to the gas-phase diatomic hydrogen molecule, is plotted across the xy -plane in Figures 3(i), 4(i), and 5(i), respectively. The most stable adsorption site for H on the Pd (111) surface is the HCP hollow position, which is site B in Figure 3(ii), with $E_{\text{ads}}(\text{H})$ of -0.67 eV; similar stability over high coordination sites is observed on the (100) surface, where the hollow site (Figure 4(ii), site C) is preferred with $E_{\text{ads}}(\text{H})$ of -0.54 eV, and the “FCC” site (Figure 5(ii), site B) is preferred in the case of the (110) surface, with $E_{\text{ads}}(\text{H})$ of -0.56 eV. The least stable adsorption site for H on all surfaces is atop, with $E_{\text{ads}}(\text{H})$ of -0.12, -0.08 and 0.00 eV on the (111), (100) and (110) Pd surfaces, respectively. The typical reactant feed for CO₂ hydrogenation is between 1:3 to 1:9 molar ratio of CO₂ and H₂, and thus dissociated hydrogen would be readily available on the catalyst surface.^{8,19} High hydrogen mobility can be deduced from Figures 3 (i), 4(i), and 5(i), as differences in favourable E_{ads} are low along specific channels, highlighted in red. The adsorption energies for H on the Pd (111) surface (-0.67 eV) and the (110) surface (-0.56 eV) compare reasonably with the experimental work of Conrad *et al.*, who report initial heats of adsorption for $\frac{1}{2}$ H₂ of 0.45 and 0.53 eV for Pd (111) and (110) surfaces, respectively.⁴⁵ There is also good agreement with previous theoretical research as Herron *et al.* calculated atomic hydrogen adsorption energies on Pd (111) using PW91 and reported them to be -0.59, -0.56 and 0.00 eV on FCC hollow, HCP hollow and atop positions, respectively.⁴⁶ Similarly, Fonseca *et al.* used PBE in their DFT study of hydrogen adsorption on Pd (111) and observed -0.66, -0.61 and -0.50 eV adsorption energies of hydrogen atom on FCC hollow, HCP hollow and bridge position, respectively.⁴⁷

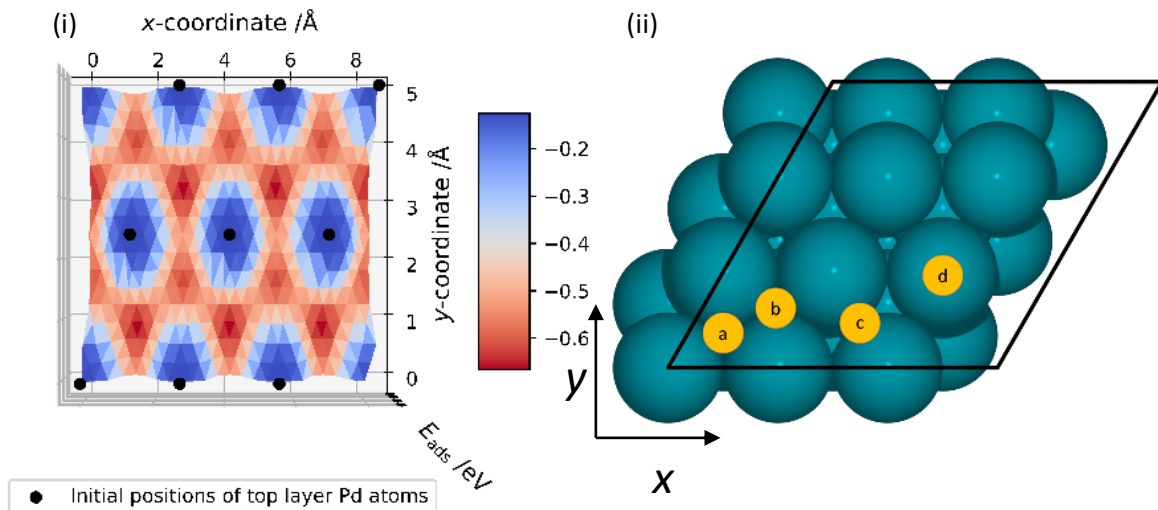


Figure 3. (i) Adsorption energy (E_{ads}) of a hydrogen atom on Pd (111) surface, calculated as a function of x - and y -coordinate; the H atom remained constrained in the xy -plane during each geometry optimisation. A key is provided for the adsorption energies, in units of eV. (ii) Top-down view of the FCC Pd (111) surface with a $3 \times 3 \times 5$ atoms simulation cell. Blue spheres represent Pd atoms and yellow circles represent unique adsorption sites: a) hollow-FCC, b) hollow-HCP, c) bridge, d) atop. Black lines represent the x - and y -direction cell boundaries.

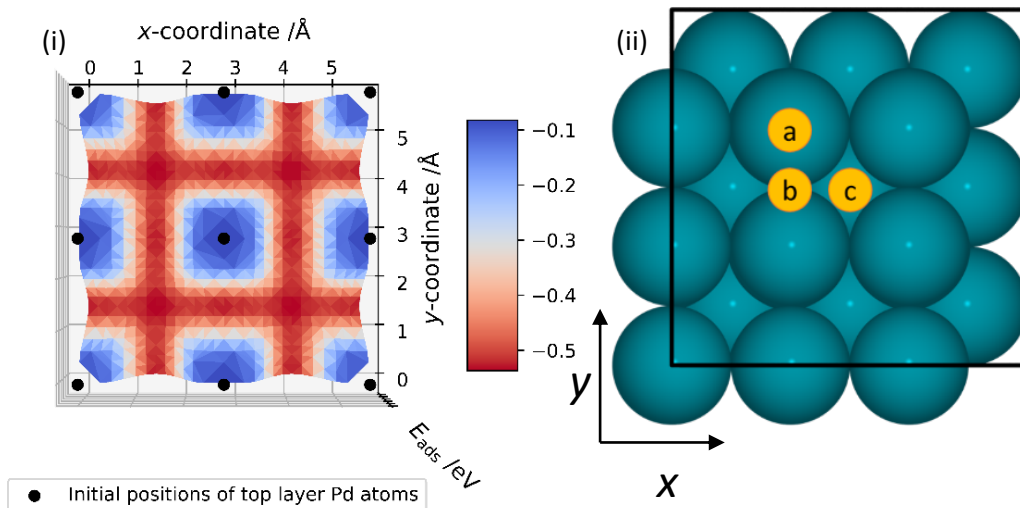


Figure 4. (i) Adsorption energy (E_{ads}) of hydrogen atom on Pd (100) surface calculated as a function of x - and y -coordinate; the H atom remained constrained in the xy -plane during each geometry optimisation. A key is provided for the adsorption energies, in units of eV. (ii) Top-down view of the FCC Pd (100) surface with a $3 \times 3 \times 5$ atoms simulation cell. Blue spheres represent Pd atoms and yellow circles represent unique adsorption sites: a) atop, b) bridge c) hollow. Black lines represent the x - and y -direction cell boundaries.

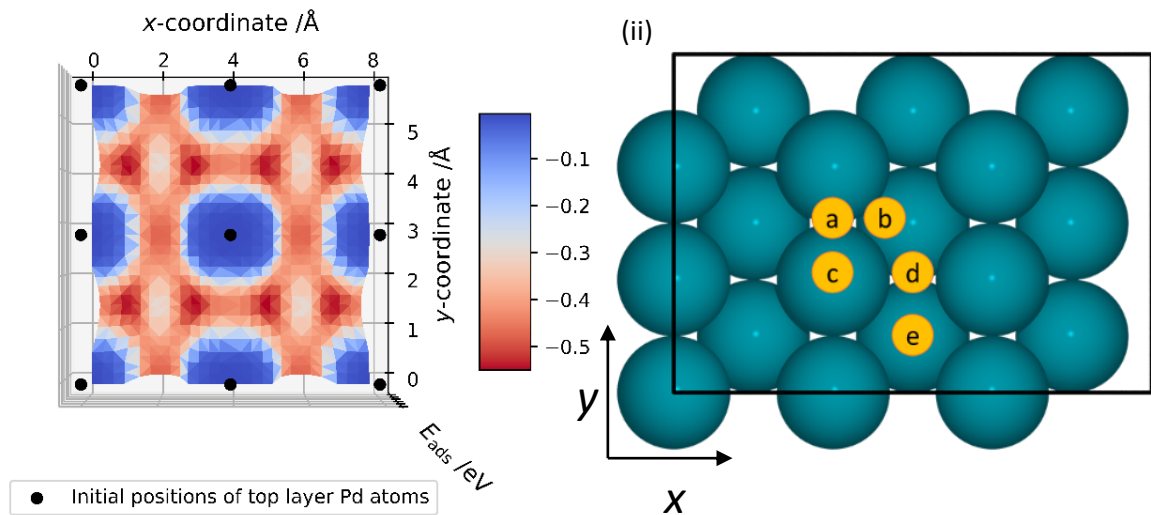


Figure 5. (i) Adsorption energy (E_{ads}) of hydrogen atom on Pd (111) surface calculated as a function of x- and y-coordinate; the H atom remained constrained in the xy-plane during each geometry optimisation. A key is provided for the adsorption energies, in units of eV. (ii) Top-down view of the FCC Pd (110) surface with a 3 x 3 x 5 atoms simulation cell. Blue spheres represent Pd atoms and yellow circles represent unique adsorption sites: a) short bridge, b) "FCC" c) atop, d) long bridge, e) hollow. Black lines represent the x- and y-direction cell boundaries.

3.2 CO₂ adsorption

The adsorption energies and structures for CO₂ on the Pd (111), (100) and (110) surfaces are reported in Table 2. The undistorted CO₂ is most stable with a C-Pd bond distance, $d_{(C-Pd)}$, of 3.454 Å, which agrees with the physisorbed species observed by Habas *et al.*²¹ $E_{ads}(CO_2)$ is strongest on the close-packed (111) surface, and is found to relate linearly with the number of Pd atoms that neighbour the surface adsorption site; when $E_{ads}(CO_2)$ is plotted as a function of surface atom coordination number, which are 9, 8, and 7 for the Pd (111), (100), and (110) surfaces, respectively, a linear fit returns $R^2 = 0.998$.

The stronger physisorption, rather than chemisorption, observed for CO₂ on the Pd (111) surface ($E_{ads}(CO_2) = -0.21$ eV) was reported previously by Ko *et al.*²¹ (-0.33 eV); they also identify a chemisorbed state CO₂^{δ-} with $E_{ads} = -0.16$ eV,¹⁷ which agrees with our observation of $E_{ads}(CO_2^{δ-}) = 0.06$ eV. Similarly, Huš *et al.* observed that on Cu catalysts CO₂ binds to the metal surface in a bent geometry, where one of the oxygens binds to a secondary metal atom and the carbon binds to a metal atom underneath.²⁴ Energy differences between our results and those of Ko *et al.* are likely due to the choice of Van der Waals correction;²⁰ never-the-less, the observed trends are very similar, and the stability of the physisorbed CO₂ implies that there is an energy barrier on the Pd (111) surface for the activation of CO₂.

Table 2. Geometric and energetic observations for CO₂ and CO₂^{δ-} physisorbed and chemisorbed species on low-index Pd surfaces, respectively; CO₂^{TS} is the transition state geometry between these stable local minima. E_{ads} is the species adsorption energy, given in eV; $d_{(C-Pd)}$ is the distance between the carbon and the nearest neighbouring Pd given in Å, and \angle_{O-C-O} is the angle between the oxygen, carbon and oxygen, given in °.

Species	Pd surface								
	111			100			110		
	E_{ads}	$d_{(C-Pd)}$	\angle_{O-C-O}	E_{ads}	$d_{(C-Pd)}$	\angle_{O-C-O}	E_{ads}	$d_{(C-Pd)}$	\angle_{O-C-O}
CO ₂	-0.21	3.45	179.5	-0.18	3.28	179.1	-0.16	3.26	179.2
CO ₂ ^{TS}	0.09	2.37	154.8	-0.02	2.45	160.6	No energy barrier		
CO ₂ ^{δ-}	0.06	2.10	140.3	-0.13	2.06	140.6	-0.23	2.06	140.2

$E_{ads}(CO_2^{δ-})$ is endothermic (0.06 eV) on the Pd (111) surface, matching the work of Zhang *et al.*²⁶, and then exothermic (-0.13 and -0.23 eV) on the Pd (100) and (110) surfaces, respectively.²⁷

$E_{ads}(CO_2^{δ-})$ is noted as increasingly negative (i.e. strengthens) with increasing E_{surf} for the Pd facets, and the energy difference between surface-bound CO₂ and CO₂^{δ-} also decreases; these observations agree with experimental data that show an absence of chemisorption on the Pd (111) surface, and both physisorption and chemisorption on the Pd (100) surface.¹¹⁻¹³ Despite differences in $E_{ads}(CO_2^{δ-})$ on the considered surfaces, the adsorbed geometries of CO₂ and CO₂^{δ-} are consistent across all considered surfaces (Table 2); only a small differences in angles (0.4°) exists for either the physisorbed or chemisorbed geometries when compared across the three facets.

Mulliken charge analysis of the CO_2 and $\text{CO}_2^{\delta-}$ species adsorbed on the Pd (111), (110) and (100) facets provides insight into the electronic charge of surface species, and the data acquired are reported in Table 3. The notation used for describing charges on atoms of interest is shown in Figure 6: O^1 and O^2 are oxygen atoms on CO_2 molecule; the two closest Pd atoms interacting with CO_2 are labelled Pd^1 and Pd^2 , where Pd^1 is closest to O^1 and Pd^2 is closest to O^2 ; and Pd_{surf} , $\text{Pd}_{\text{sublayer}}$, and Pd_{slab} refer to the first, second and all layers of Pd atoms in the model, respectively.

Table 3. Net Mulliken charges, in units of e , on relevant atoms for CO_2 physisorption and chemisorption on the Pd (111), (110) and (100) surfaces; the charges (q) have been averaged over Pd atoms in the first surface layer surface (Pd_{surf}) and sublayer ($\text{Pd}_{\text{sublayer}}$), as well as over the whole slab (Pd_{slab}).

	CO_2				$\text{CO}_2^{\delta-}$		
	Gas	Pd (111)	Pd (110)	Pd (100)	Pd (111)	Pd (110)	Pd (100)
q_C	+0.48	+0.47	+0.45	+0.44	+0.39	+0.38	+0.38
q_{O^1}	-0.24	-0.22	-0.22	-0.22	-0.19	-0.26	-0.23
q_{O^2}	-0.24	-0.23	-0.22	-0.22	-0.23	-0.24	-0.25
q_{Pd^1}	-	-0.02	-0.05	-0.05	-0.32	-0.10	-0.15
q_{Pd^2}	-	-0.01	-0.02	0.00	-0.30	+0.04	-0.07
$q_{\text{Pd}_{\text{sublayer}}}$	-	+0.02	+0.05	0.00	-0.02	+0.03	+0.00
$q_{\text{Pd}_{\text{surf}}}$	-	-0.00	-0.01	0.00	-0.07	+0.00	-0.02
$q_{\text{Pd}_{\text{slab}}}$	-	-0.02	-0.01	0.00	+0.04	+0.11	+0.10

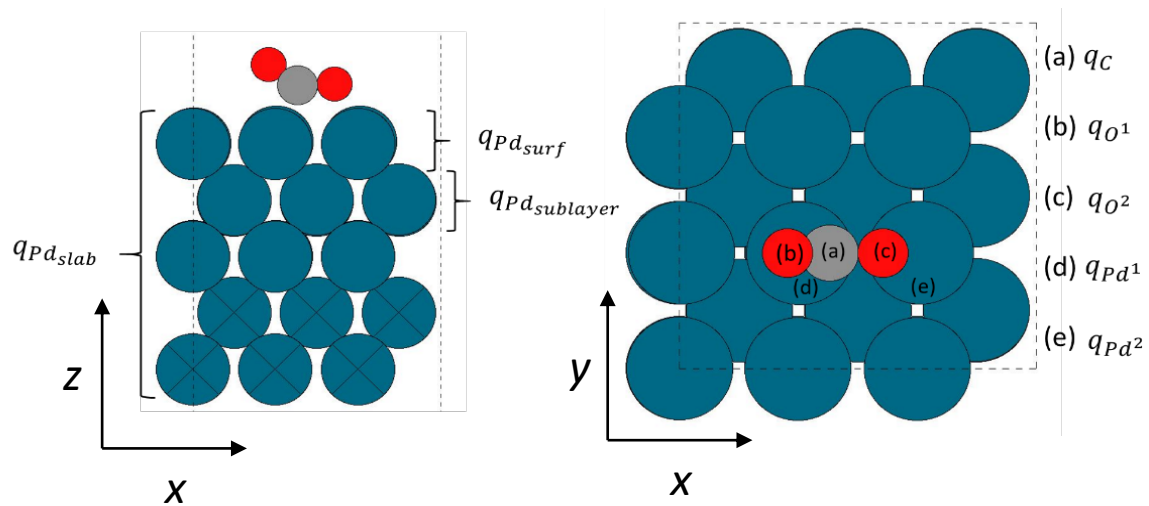


Figure 6. Side- and top-view of CO_2 chemisorbed on the FCC Pd (100) surface, illustrating notations used for Mulliken analysis. Blue, red, and grey spheres represent Pd, O, and C atoms, respectively. Black crosses mark constrained bulk Pd layers, and dashed lines illustrate the boundary of the surface supercell.

For CO_2 physisorption on the Pd (111) surface (Figure 7a), the charge of the carbon (q_C) is +0.47 e , very similar to the gas phase CO_2 ($q_C = +0.48$ e), and only small changes are observed on the surface Pd. For $\text{CO}_2^{\delta-}$ on the Pd (111) surface (Figure 7b), negatively charged Pd atoms bond to an oxygen and carbon ($q_{\text{Pd}^1} = -0.30$ e , $q_{\text{Pd}^2} = -0.32$ e). The distance $d_{(\text{C}-\text{Pd}^2)}$ is 2.85 \AA , and there is a direct electronic

interaction between Pd² and the carbon atom of CO₂. For chemisorbed CO₂^{δ-}, the overall charge on the second layer of Pd atoms, $q_{Pd_{sublayer}}$, decreases from +0.14 to -0.15 e, whereas the charge on the first surface atomic layer of Pd, $q_{Pd_{surf}}$, has changed from -0.02 to -0.66 e, suggesting that the electron density has been pulled to the first two layers of Pd, and to the CO₂^{δ-} adsorbate *via* Pd¹ and Pd². q_C has decreased from +0.47 e to +0.39 e, indicating some metal (Pd¹) to empty CO₂ π* orbital electron transfer.¹¹ The negatively charged oxygen in proximity to the negative q_{Pd^1} and q_{Pd^2} will result in electrostatic Pauli repulsion, and thus are likely to contribute in the decreased stability of CO₂^{δ-} on the Pd (111) surface.^{21,48}

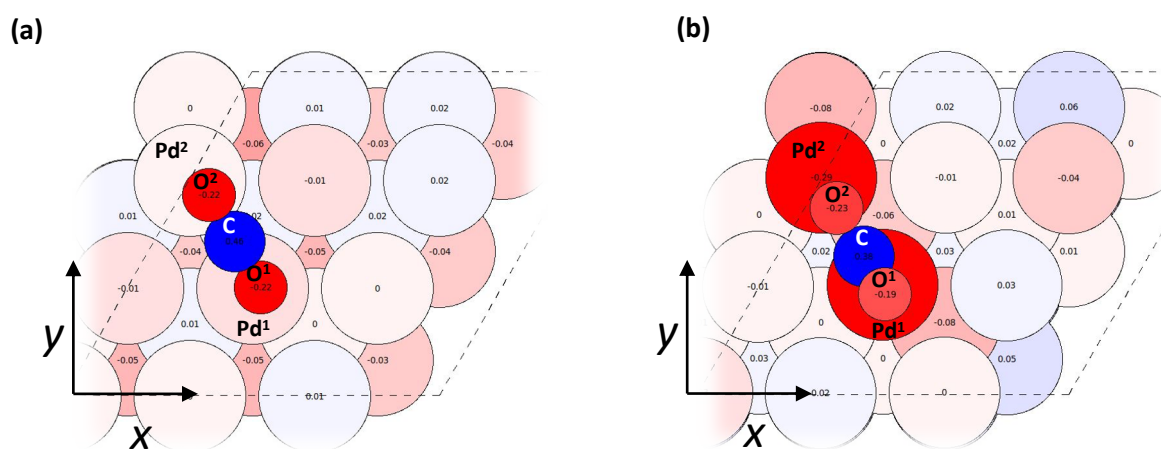


Figure 7. A red-white-blue (negative-neutral-positive charges) color-coded visualisation of the net Mulliken charge on atoms for (a) CO₂ physisorbed and (b) CO₂^{δ-} chemisorbed on the Pd (111) surface.

In contrast, for CO₂ physisorbed on the Pd (110) surface (Figure 8), $q_C = +0.45$ e; for CO₂^{δ-} on Pd (110), q_C reduces to +0.38 e, similar to for the (111) surface, though with a higher electron density on the oxygens that contributes to the overall stability (i.e. lower E_{ads}). Significantly for the (110) surface, only Pd¹, which is directly below the CO₂ carbon, is negatively charged ($q_{Pd^1} = -0.10$ e), demonstrating much lesser charge redistribution than on the Pd (111) surface. The differing charge transfer provides insight as to why the CO₂^{δ-} on the Pd (110) surface is more stable than on Pd (111).

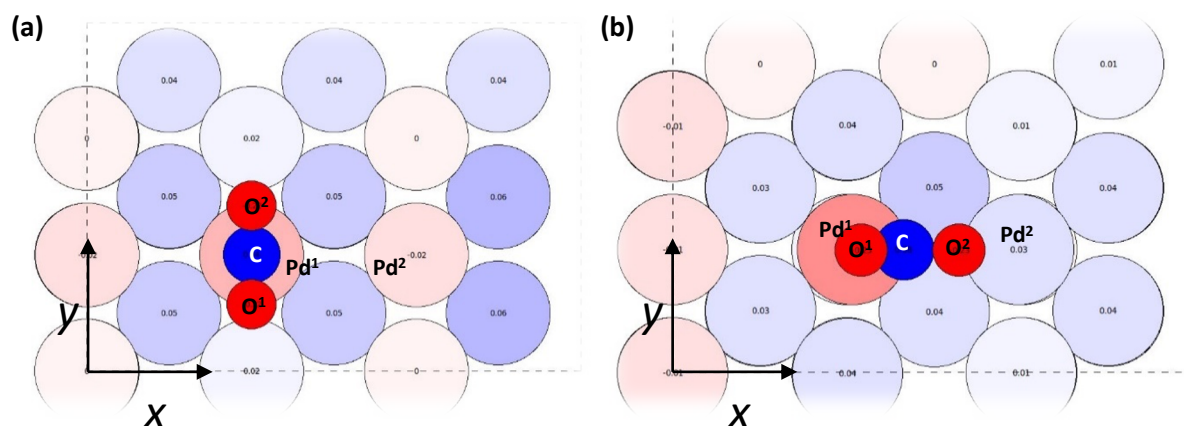


Figure 8. A red-white-blue (negative-neutral-positive charges) color-coded visualisation of the net Mulliken charge on atoms for (a) CO₂ and (b) CO₂^{δ-} on the Pd (110) surface.

For CO₂^{δ-} on a Pd (100) facet (Figure 9), the charges calculated are intermediary to the results on the Pd (111) and (110) surfaces: E_{ads} of chemisorbed CO₂^{δ-} and physisorbed CO₂ on Pd (100) are similar; and a negative charge accumulates on the carbon-bound Pd ($q_{\text{Pd}^1} = -0.15$ e), with a small negative charge on the oxygen-bound Pd ($q_{\text{Pd}^2} = -0.07$ e). The coordination of Pd (100) surface atoms is lower than that of atoms on the Pd (111) surface, which results in lower stability for the physisorbed CO₂.

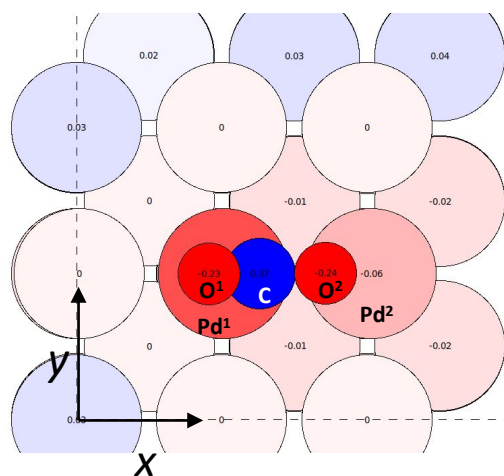


Figure 9. A red-white-blue (negative-neutral-positive charges) color-coded visualisation of the net Mulliken charge on atoms for the CO₂^{δ-} on the Pd (100) surface.

The overall charge transfer from the metal to CO₂^{δ-} is -0.04, -0.10 and -0.12 e on Pd (111), (100) and (110) surfaces, respectively, in correlation with adsorption strength. In previous literature, Bader charge analysis has been considered for CO₂ chemisorption on Pd (111) surfaces, and the transfer to CO₂^{δ-} reported as -0.28 and -0.43 e by Tang *et al.* and Habas *et al.*, respectively;^{21,49} the direction of charge transfer is consistent with our own observations, with the quantitative difference attributed to method differences. Importantly, we show qualitatively that the charge transfer to CO₂^{δ-} increases over Pd (111), (100), and (110) surfaces, indicating that Pd (100) and (110) surfaces are more suitable for CO₂ activation than the most stable Pd (111) surface.

3.3 Interactions of intermediates with Pd surfaces.

Reaction intermediates from the Grabow mechanism, as introduced in Section 1.2, have been optimised on the pristine Pd (111), (100) and (110) surfaces, in each case starting from an atop position. The calculated values of E_{ads} are presented in Figure 10.

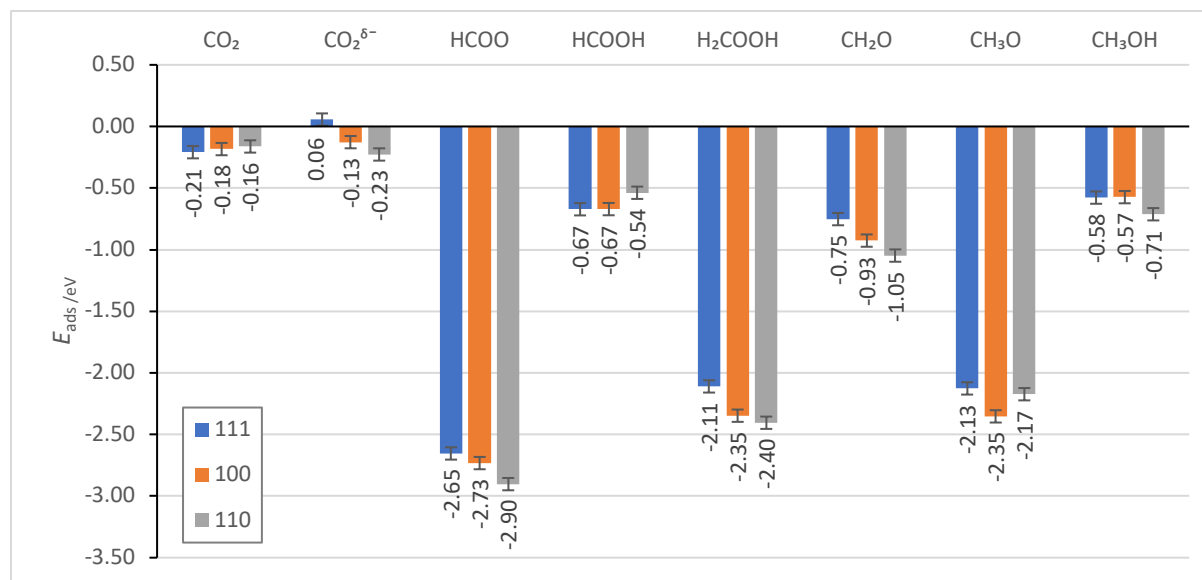


Figure 10. E_{ads} of the intermediates in the direct CO_2 hydrogenation to methanol, as studied on the low-index Pd surfaces, presented in order of increasing E_{surf} : (111), (100) and (110),²⁵ in blue, orange and grey, respectively. Error bars of ± 0.05 eV are provided to account for the spin-paired approximation applied to the adsorbed species, as described in Section 2.3.

For the intermediates considered, the average difference between the highest and lowest E_{ads} across the three surfaces is 0.23 eV; the smallest difference is for the HCOOH and CH_3OH molecules (0.13 and 0.14 eV, respectively), and the largest for H_2CO (0.30 eV). Plotting the surface energy (E_{surf}) of the low-index Pd surfaces against the adsorption energy (E_{ads}) of these intermediates on the corresponding surfaces (Figure 11) illustrates how trends in surface properties associate with the observations. In particular, E_{ads} of $\text{CO}_2^{\delta-}$, HCOO, H_2COOH and H_2CO present clear linear correlations with the stability of the surface facets, giving R^2 of 0.997, 0.823, 0.986 and 0.986, respectively. HCOOH, H_3CO and CH_3OH give a poor linear fit, which indicates that other factors, such as steric effects, should be considered for rationalising the strength of these adsorbate interactions with the Pd surfaces. For example, due to additional space on the long-bridge site on the Pd (110) surface, the HCOOH can be accommodated in a different orientation from that on the Pd (111) and (100) surfaces (i. e. C-H atoms facing down, rather than up), which makes the resulting structures more difficult to compare directly.

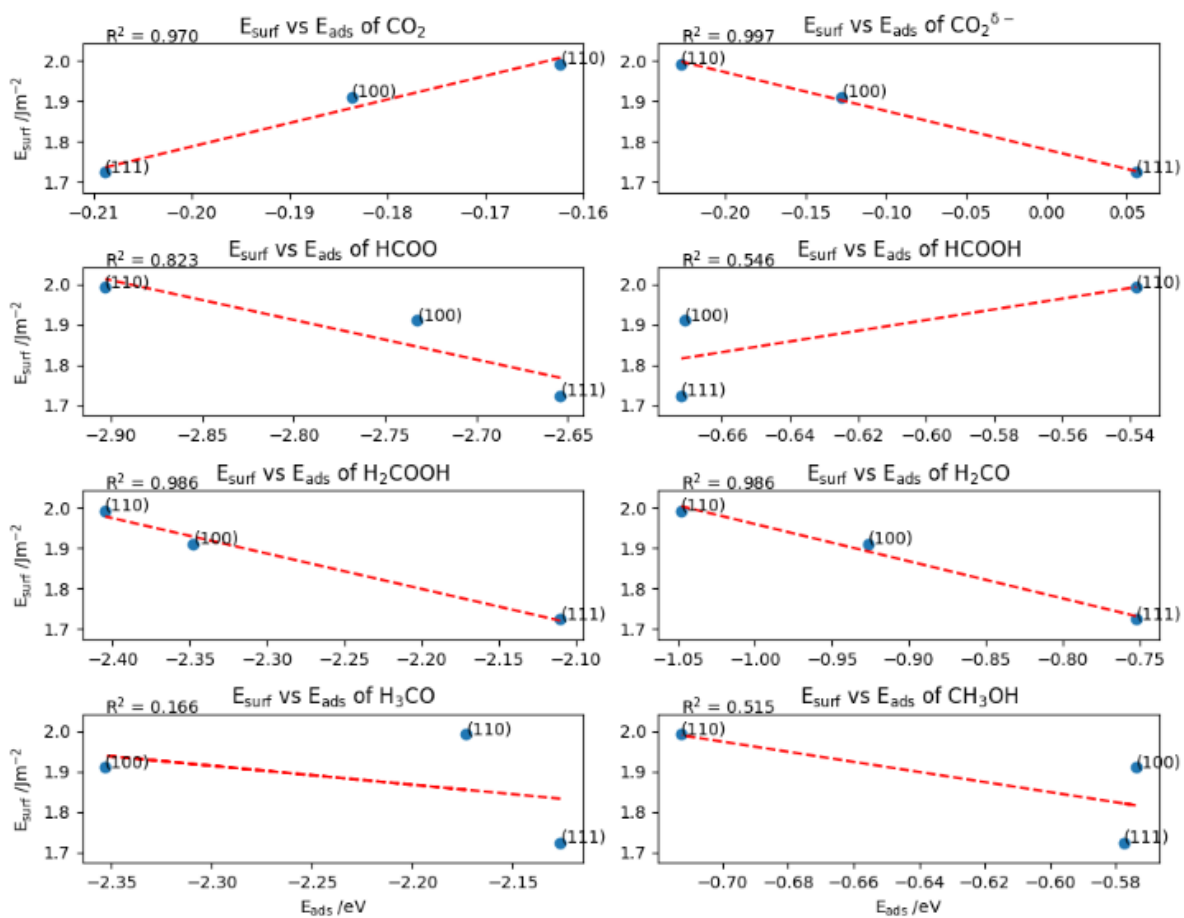


Figure 11. E_{surf} of the Pd (111), (100) and (110) surfaces plotted against E_{ads} of intermediates in the mechanism of CO_2 hydrogenation to methanol. The red dashed line is the linear fit of the data points, and R^2 is the linear coefficient of determination showing the quality of the fit.

3.4 Transition states and reaction profile

In order to determine reaction kinetics, activation energies were calculated. Here, for each reaction step that involved a hydrogenation, it was necessary to set the transition state (TS) starting geometry such that a hydrogen atom was positioned near to the intermediate; optimisation of these starting models with proximal hydrogen in some instances led to instability of the intermediate adsorption structures, though did not cause issues when directly applied to the TS calculations. Once a transition state structure was confirmed, the activation energy (E_{act}) was calculated for each reaction step as:

$$E_{\text{act}} = E_{\text{TS}}(\text{species}) - E_{\text{ads}}(\text{species}) \quad \text{Equation 7.}$$

The resulting E_{act} are presented in Figure 12, and tabulated in the SI. Here, $\text{CO}_2^{\delta-}$ was considered as the starting point, i.e. proceeding via a Langmuir-Hinshelwood mechanism, and *not* a physisorbed CO_2 akin to an Eley-Rideal mechanism.²⁵ As part of the reaction pathway via formate, the decomposition of H_2COOH^* into H_2CO^* and OH^* was included, as previously considered for metal catalysts containing Cu, Pd and Zn.^{23–25,50}

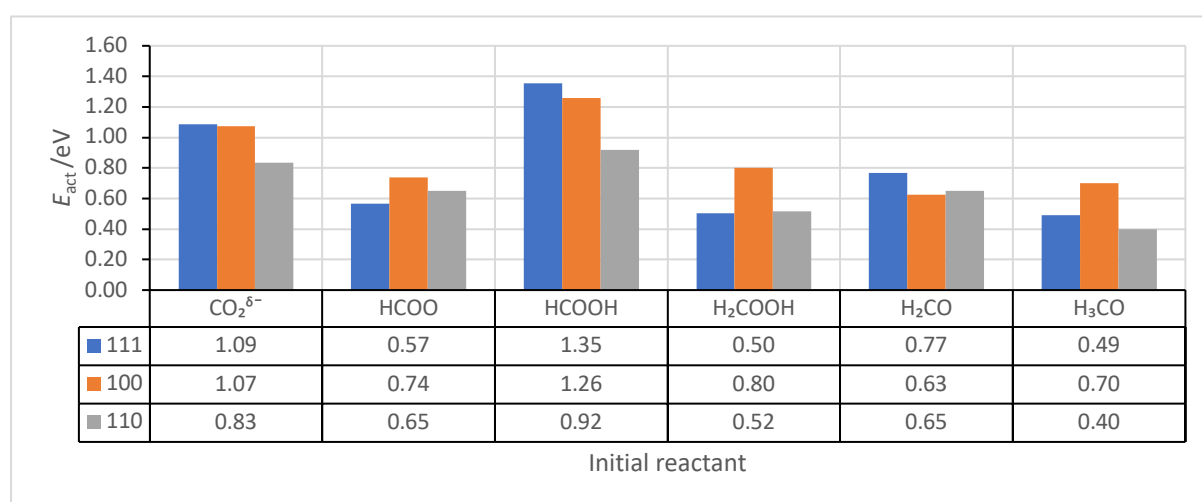


Figure 12. The activation energies (E_{act} , eV) of reaction steps in the pathway for CO_2 hydrogenation to methanol, presented for Pd surfaces in order of increasing E_{surf} , i.e. (111), (100), and (110), given in blue, orange, and grey, respectively. In each case, the label refers to the initial reaction species, and the activation energies are also tabulated.

The activation energy for $\text{CO}_2^{\delta-}$ hydrogenation, $E_{\text{act}}(\text{CO}_2^{\delta-})$, is 1.09 eV, 1.07 eV and 0.83 eV on the Pd (111), (100) and (110) surfaces, respectively. The observation that $E_{\text{act}}(\text{CO}_2^{\delta-})$ is lowest on the Pd (110) surface can be attributed to the additional space underneath the $\text{CO}_2^{\delta-}$ on the preferred long-bridge site, which facilitates the hydrogen atom binding to the carbon. The $E_{\text{act}}(\text{CO}_2^{\delta-})$ on the Pd (111) surface reported (1.09 eV) matches the work of Zhang *et al.* (0.85 eV), though differs somewhat from the results of Brix *et al.* (2.23 eV); we believe this difference stems from use of a physisorbed CO_2 geometry

in their calculations, i.e. an Eley-Rideal mechanism, with a chemisorbed structure considered in our work and the calculations by Zhang *et al.*^{26,50}

$E_{\text{act}}(\text{HCOOH})$ is observed to decrease with increasing E_{surf} , i.e. follows the trend (111) > (100) > (110). The highest $E_{\text{act}}(\text{HCOOH})$ of 1.35 eV, calculated for the Pd (111) surface, is in agreement with the value of 1.13 eV reported by Brix *et al.* Given that the adsorption energy of HCOOH on the Pd (111) surface is calculated as -0.67 eV, and desorption is considered as the reverse process, the high $E_{\text{act}}(\text{HCOOH})$ observed (1.35 eV) for the Pd (111) surface suggests that HCOOH is more likely to desorb than react further. The high activation barrier for HCOOH hydrogenation agrees with work by Huš *et al.* on Cu-based catalysts; however, formic acid is not amongst the product stream observed when using Pd catalysts experimentally, with CH₃OH, CO and trace to significant amounts of CH₄ reported.^{4,8,19,24,51} Thus, another intermediate, such as H₂COO, might be of importance in leading to the experimental products, as was determined for Cu-based catalysts.²⁴ In our work, the $E_{\text{act}}(\text{HCOOH})$ on the Pd (110) surface is about 30 % lower than on Pd (111), which might stem from lower stability of the HCOOH, and reduced stability of the hydrogen atom on Pd (110), which translates into a more accessible transition state.

The activation energy for dissociation of H₂COOH species, $E_{\text{act}}(\text{H}_2\text{COOH})$, is highest on the Pd (100) surface, where the H₂COOH intermediate is stabilised. Brix *et al.* reported a very high $E_{\text{act}}(\text{H}_2\text{COOH})$ of 2.01 eV on Pd (111), while we observe $E_{\text{act}}(\text{H}_2\text{COOH})$ to be only 0.50 eV. For hydrogenation of formaldehyde, $E_{\text{act}}(\text{H}_2\text{CO})$ is similarly low (0.63 – 0.77 eV) on the three surfaces; however, on the (111) surface it is very close to the E_{ads} of H₂CO (-0.75 eV), whilst on Pd (100) and (110) surfaces, H₂CO is stabilised more (-0.93 and -1.05 eV) than on Pd (111). The stronger E_{ads} on (100) and (110) surfaces means H₂CO desorption is unlikely, and reactivity favoured, whilst on the (111) surface desorption would be a competitive process. Desorption of H₂CO during CO₂ hydrogenation to methanol on Pd catalysts is a major concern in experiment,⁴ which suggests that Pd (100) and (110) surfaces are preferable in catalyst design.

In the majority of hydrogenation steps examined on all three Pd surfaces, the reaction pathway favoured migration of the hydrogen atom towards the least stable on-top site before bonding to the intermediate. Therefore, the relative stability of the hydrogen adsorption sites, as shown in Section 3.1, has a major impact on the E_{act} for most hydrogenation reactions on the Pd (111), (100) and (110) surfaces. Reducing the difference in stability for hydrogen atoms on the possible surface sites might be an important factor in the design of catalysts for CO₂ hydrogenation to methanol, as this could lead to reduction of E_{act} for species reacting on a Pd-based catalyst.

A reaction profile based on the energy of initial, TS and final geometries, relative to the energy of isolated Pd (111), (100) and (110) surfaces and gas-phase reactants, is plotted in Figure 13, with each individual step balanced stoichiometrically by energies of gas-phase molecules.

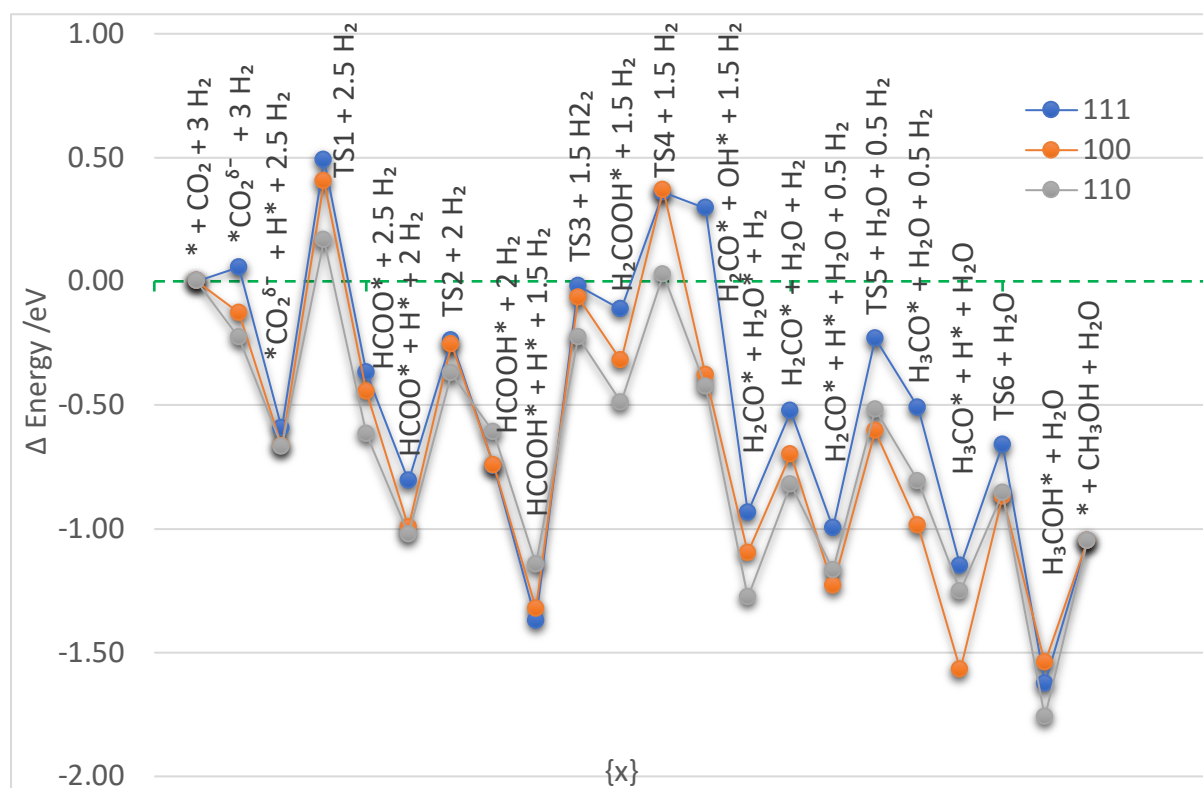


Figure 13. The energy profile of CO₂ hydrogenation to methanol, *via* the formate pathway, on Pd (111), (100), and (110) surfaces, plotted in blue, orange, and grey, respectively, relative to the energy of pristine surface and gas phase reactants.²⁵ Energies of intermediate structures and transition state geometries have been stoichiometrically balanced with energies of gas phase reactants; * indicates surface bound species.

Over all the surfaces, the conversion of CO₂ to methanol reaction energy is exothermic (-1.05 eV) relative to gas phase reactants, which agrees with experimental reaction energy (-1.17) derived from static-nuclei formation energies.^{4,52,53} The highest E_{act} in the CO₂ hydrogenation reaction across the Pd (111), (100) and (110) surfaces is $E_{act}(\text{HCOOH})$, with values of 1.35, 1.26, and 0.92 eV, respectively; thus, this is considered to be the rate determining step (RDS) of the reaction. An important feature of the reaction energy profile is that TS1 remains endothermic on all three surfaces, with respect to the gas phase reactants, which would inevitably influence the rate of the reaction. All transition states on Pd (110) remain close to or below net zero energy of the reaction, which indicates that Pd (110) is the most active among the surfaces investigated here. As highlighted in Section 3.1, the hydrogen atoms are stabilised strongly on the Pd (111), (100), and (110) surfaces; the binding energies of intermediates with a neighbouring hydrogen atom do not vary significantly from the sum of binding energies of the adsorbates calculated separately, which suggests that the presence of hydrogen neither stabilises nor destabilises the intermediates at the low monolayer coverage (1/9 ML) of hydrogen considered.²⁵

4. Summary and Conclusions

Direct hydrogenation of CO₂ to methanol on transition metal catalysts is a promising way of green energy storage, and in order to make the technology viable, new and more efficient catalysts need to be designed. Here, we have investigated the CO₂ hydrogenation reaction *via* the formate pathway on Pd (111), (100), and (110) surfaces. Firstly, we investigated the stability of H on the Pd surfaces, showing that high coordination sites have the largest adsorption energy, and these high stability sites are interlinked via channels with low diffusion barriers; we also show for CO₂ adsorption that the preference of physical or chemical adsorption is dependent on the stability of the Pd surface facet.

For the CO₂ hydrogenation reaction, the transition state for CO₂^{δ-} hydrogenation (TS1), to form formate, is endothermic, which will influence the overall rate of the reaction. $E_{\text{act}}(\text{HCOOH})$ is the highest energy step in the reaction profile on the Pd (111), (100), and (110) surfaces (TS3), and it can be considered as the rate determining step of this reaction on the surfaces examined. Novel Pd-based polymetallic nanoparticle catalysts for direct CO₂ hydrogenation to methanol could be designed to lower the barrier to initial CO₂ hydrogenation, TS1, and also lower the barrier for formic acid hydrogenation (TS3) or facilitate a mechanism that proceeds *via* an alternative intermediate, such as H₂COO.

Overall, we show that the most stable geometry of CO₂ adsorbed on Pd surface varies across (111), (100) and (110) facets and future studies should not be limited to consideration of the lowest energy (111) surface facet. The H₂COO intermediate could be alternatively considered as part of the formate pathway. Future work will entail modelling of the reaction on multi-component Pd-based catalytic systems, which have been shown to manifest great selectivity to CH₃OH in direct CO₂ hydrogenation.^{19,54–56}

5. Conflicts of interest

There are no conflicts of interest to declare.

6. Acknowledgements

The authors are grateful for funding by the EPSRC Centre-to Centre Project (Grant reference: EP/S030468/1). IK acknowledges the Cardiff School of Chemistry for a PhD studentship award. We are grateful to Matthias Scheffler, Yuanyuan Zhou, Herzain Rivera, Graham Hutchings, Mike Bowker and David Willock for useful discussions. AJL acknowledges funding by the UKRI Future Leaders Fellowship program (MR/T018372/1). The authors acknowledge computational resources and support from: the Supercomputing Wales project, which is part-funded by the European Regional Development Fund (ERDF) via the Welsh Government; the UK National Supercomputing Services ARCHER and ARCHER2, accessed via membership of the Materials Chemistry Consortium, which is funded by Engineering and Physical Sciences Research Council (EP/L000202/1, EP/R029431/1, EP/T022213/1); and the Isambard UK National Tier-2 HPC Service operated by GW4 and the UK Met Office, and funded by EPSRC (EP/P020224/1).

7. References

- (1) Hutchings, G.; Davidson, M.; Atkins, P.; Collier, P.; Jackson, N.; Morton, A.; Muskett, M.; Rosseinsky, M.; Styring, P.; Thornley, P.; Williams, C. *Sustainable Synthetic Carbon Based Fuels for Transport: Policy Briefing*; The Royal Society, 2019.
- (2) Roy, S.; Cherevotan, A.; Peter, S. C. Thermochemical CO₂ Hydrogenation to Single Carbon Products: Scientific and Technological Challenges. *ACS Energy Lett.* **2018**, *3* (8), 1938–1966. <https://doi.org/10.1021/acsenergylett.8b00740>.
- (3) Bussche, K. M. V.; Froment, G. F. A Steady-State Kinetic Model for Methanol Synthesis and the Water Gas Shift Reaction on a Commercial Cu/ZnO/Al₂O₃ Catalyst. *J. Catal.* **1996**, *161* (1), 1–10. <https://doi.org/10.1006/jcat.1996.0156>.
- (4) Bowker, M. Methanol Synthesis from CO₂ Hydrogenation. *ChemCatChem* **2019**, *11* (17), 4238–4246. <https://doi.org/10.1002/cctc.201900401>.
- (5) Ko, J.; Kim, B.-K.; Han, J. W. Density Functional Theory Study for Catalytic Activation and Dissociation of CO₂ on Bimetallic Alloy Surfaces. *J. Phys. Chem. C* **2016**, *120* (6), 3438–3447. <https://doi.org/10.1021/acs.jpcc.6b00221>.
- (6) Xu, J.; Su, X.; Liu, X.; Pan, X.; Pei, G.; Huang, Y.; Wang, X.; Zhang, T.; Geng, H. Methanol Synthesis from CO₂ and H₂ over Pd/ZnO/Al₂O₃: Catalyst Structure Dependence of Methanol Selectivity. *Appl. Catal. Gen.* **2016**, *514*, 51–59. <https://doi.org/10.1016/j.apcata.2016.01.006>.
- (7) Melián-Cabrera, I.; Granados, M. L.; Fierro, J. L. G. Pd-Modified Cu–Zn Catalysts for Methanol Synthesis from CO₂/H₂ Mixtures: Catalytic Structures and Performance. *J. Catal.* **2002**, *210* (2), 285–294. <https://doi.org/10.1006/jcat.2002.3677>.
- (8) Iwasa, N.; Suzuki, H.; Terashita, M.; Arai, M.; Takezawa, N. Methanol Synthesis from CO₂ Under Atmospheric Pressure over Supported Pd Catalysts. *Catal. Lett.* **2004**, *96* (1), 75–78. <https://doi.org/10.1023/B:CATL.0000029533.41604.13>.
- (9) Iwasa, N.; Mayanagi, T.; Ogawa, N.; Sakata, K.; Takezawa, N. New Catalytic Functions of Pd–Zn, Pd–Ga, Pd–In, Pt–Zn, Pt–Ga and Pt–In Alloys in the Conversions of Methanol. *Catal. Lett.* **1998**, *54* (3), 119–123. <https://doi.org/10.1023/A:1019056728333>.
- (10) Manrique, R.; Jiménez, R.; Rodríguez-Pereira, J.; Baldovino-Medrano, V. G.; Karelavic, A. Insights into the Role of Zn and Ga in the Hydrogenation of CO₂ to Methanol over Pd. *Int. J. Hydrog. Energy* **2019**, *44* (31), 16526–16536. <https://doi.org/10.1016/j.ijhydene.2019.04.206>.
- (11) Solymosi, F.; Berkó, A. Adsorption of CO₂ on Clean and Potassium-Covered Pd(100) Surfaces. *J. Catal.* **1986**, *101* (2), 458–472. [https://doi.org/10.1016/0021-9517\(86\)90273-3](https://doi.org/10.1016/0021-9517(86)90273-3).

- (12) Solymosi, F. The Bonding, Structure and Reactions of CO₂ Adsorbed on Clean and Promoted Metal Surfaces. *J. Mol. Catal.* **1991**, *65* (3), 337–358. [https://doi.org/10.1016/0304-5102\(91\)85070-I](https://doi.org/10.1016/0304-5102(91)85070-I).
- (13) Matsushima, T.; Asada, H. Kinetic Studies on the CO Oxidation on Pd(111) with Low Energy Electron Diffraction (LEED) and Angle-resolved Thermal Desorption. *J. Chem. Phys.* **1986**, *85* (3), 1658–1668. <https://doi.org/10.1063/1.451206>.
- (14) Burghaus, U. Surface Chemistry of CO₂ – Adsorption of Carbon Dioxide on Clean Surfaces at Ultrahigh Vacuum. *Prog. Surf. Sci.* **2014**, *89* (2), 161–217. <https://doi.org/10.1016/j.progsurf.2014.03.002>.
- (15) Kao, C.-L.; Carlsson, A.; Madix, R. J. The Adsorption Dynamics of Molecular Carbon Dioxide on Pt(111) and Pd(111). *Surf. Sci.* **2002**, *497* (1), 356–372. [https://doi.org/10.1016/S0039-6028\(01\)01674-0](https://doi.org/10.1016/S0039-6028(01)01674-0).
- (16) Liu, X.; Sun, L.; Deng, W.-Q. Theoretical Investigation of CO₂ Adsorption and Dissociation on Low Index Surfaces of Transition Metals. *J. Phys. Chem. C* **2018**, *122* (15), 8306–8314. <https://doi.org/10.1021/acs.jpcc.7b12660>.
- (17) Brosseau, R.; Ellis, T. H.; Wang, H. The Influence of Water on the Chemisorption of CO₂ onto Pd(110). *Chem. Phys. Lett.* **1991**, *177* (2), 118–122. [https://doi.org/10.1016/0009-2614\(91\)90055-E](https://doi.org/10.1016/0009-2614(91)90055-E).
- (18) Erdöhelyi, A.; Pásztor, M.; Solymosi, F. Catalytic Hydrogenation of CO₂ over Supported Palladium. *J. Catal.* **1986**, *98* (1), 166–177. [https://doi.org/10.1016/0021-9517\(86\)90306-4](https://doi.org/10.1016/0021-9517(86)90306-4).
- (19) Bahruji, H.; Bowker, M.; Hutchings, G.; Dimitratos, N.; Wells, P.; Gibson, E.; Jones, W.; Brookes, C.; Morgan, D.; Lalev, G. Pd/ZnO Catalysts for Direct CO₂ Hydrogenation to Methanol. *J. Catal.* **2016**, *343*, 133–146. <https://doi.org/10.1016/j.jcat.2016.03.017>.
- (20) Ko, J.; Kim, B.-K.; Han, J. W. Density Functional Theory Study for Catalytic Activation and Dissociation of CO₂ on Bimetallic Alloy Surfaces. *J. Phys. Chem. C* **2016**, *120* (6), 3438–3447. <https://doi.org/10.1021/acs.jpcc.6b00221>.
- (21) Habas, M.-P.; Mele, F.; Sodupe, M.; Illas, F. Density Functional Cluster Model Study of Bonding and Coordination Modes of CO₂ on Pd(111). *Surf. Sci.* **1999**, *431* (1), 208–219. [https://doi.org/10.1016/S0021-9517\(99\)00055-5](https://doi.org/10.1016/S0021-9517(99)00055-5).
- (22) Medford, A. J.; Sehested, J.; Rossmeisl, J.; Chorkendorff, I.; Studt, F.; Nørskov, J. K.; Moses, P. G. Thermochemistry and Micro-Kinetic Analysis of Methanol Synthesis on ZnO (0001). *J. Catal.* **2014**, *309*, 397–407. <https://doi.org/10.1016/j.jcat.2013.10.015>.

- (23) Kattel, S.; Ramírez, P. J.; Chen, J. G.; Rodriguez, J. A.; Liu, P. Active Sites for CO₂ Hydrogenation to Methanol on Cu/ZnO Catalysts. *Science* **2017**, *355* (6331), 1296–1299. <https://doi.org/10.1126/science.aal3573>.
- (24) Huš, M.; Kopač, D.; Štefančič, N. S.; Jurković, D. L.; Dasireddy, V. D. B. C.; Likozar, B. Unravelling the Mechanisms of CO₂ Hydrogenation to Methanol on Cu-Based Catalysts Using First-Principles Multiscale Modelling and Experiments. *Catal. Sci. Technol.* **2017**, *7* (24), 5900–5913. <https://doi.org/10.1039/C7CY01659J>.
- (25) Grabow, L. C.; Mavrikakis, M. Mechanism of Methanol Synthesis on Cu through CO₂ and CO Hydrogenation. *ACS Catal.* **2011**, *1* (4), 365–384. <https://doi.org/10.1021/cs200055d>.
- (26) Zhang, M.; Wu, Y.; Dou, M.; Yu, Y. A DFT Study of Methanol Synthesis from CO₂ Hydrogenation on the Pd(111) Surface. *Catal. Lett.* **2018**, *148* (9), 2935–2944. <https://doi.org/10.1007/s10562-018-2497-y>.
- (27) Blum, V.; Gehrke, R.; Hanke, F.; Havu, P.; Havu, V.; Ren, X.; Reuter, K.; Scheffler, M. Ab Initio Molecular Simulations with Numeric Atom-Centered Orbitals. *Comput. Phys. Commun.* **2009**, *180* (11), 2175–2196. <https://doi.org/10.1016/j.cpc.2009.06.022>.
- (28) Larsen, A. H.; Mortensen, J. J.; Blomqvist, J.; Castelli, I. E.; Christensen, R.; Du\lak, M.; Friis, J.; Groves, M. N.; Hammer, B.; Hargus, C.; Hermes, E. D.; Jennings, P. C.; Jensen, P. B.; Kermode, J.; Kitchin, J. R.; Kolsbjerg, E. L.; Kubal, J.; Kaasbjerg, K.; Lysgaard, S.; Maronsson, J. B.; Maxson, T.; Olsen, T.; Pastewka, L.; Peterson, A.; Rostgaard, C.; Schiøtz, J.; Schütt, O.; Strange, M.; Thygesen, K. S.; Vegge, T.; Vilhelmsen, L.; Walter, M.; Zeng, Z.; Jacobsen, K. W. The Atomic Simulation Environment—a Python Library for Working with Atoms. *J. Phys. Condens. Matter* **2017**, *29* (27), 273002. <https://doi.org/10.1088/1361-648X/aa680e>.
- (29) Ernzerhof, M.; Scuseria, G. E. Assessment of the Perdew–Burke–Ernzerhof Exchange–Correlation Functional. *J. Chem. Phys.* **1999**, *110* (11), 5029–5036. <https://doi.org/10.1063/1.478401>.
- (30) Tkatchenko, A.; Scheffler, M. Accurate Molecular Van Der Waals Interactions from Ground-State Electron Density and Free-Atom Reference Data. *Phys. Rev. Lett.* **2009**, *102* (7), 073005. <https://doi.org/10.1103/PhysRevLett.102.073005>.
- (31) Monkhorst, H. J.; Pack, J. D. Special Points for Brillouin-Zone Integrations. *Phys. Rev. B* **1976**, *13* (12), 5188–5192. <https://doi.org/10.1103/PhysRevB.13.5188>.
- (32) Arblaster, J. W. Crystallographic Properties of Palladium <https://www.ingentaconnect.com/content/matthey/pmr/2012/00000056/00000003/art00006> (accessed Oct 25, 2019). <https://doi.org/info:doi/10.1595/147106712X646113>.

- (33) Janthon, P.; Luo, S. (Andy); Kozlov, S. M.; Viñes, F.; Limtrakul, J.; Truhlar, D. G.; Illas, F. Bulk Properties of Transition Metals: A Challenge for the Design of Universal Density Functionals. *J. Chem. Theory Comput.* **2014**, *10* (9), 3832–3839. <https://doi.org/10.1021/ct500532v>.
- (34) Methfessel, M.; Hennig, D.; Scheffler, M. Trends of the Surface Relaxations, Surface Energies, and Work Functions of the 4d Transition Metals. *Phys. Rev. B* **1992**, *46* (8), 4816–4829. <https://doi.org/10.1103/PhysRevB.46.4816>.
- (35) Vitos, L.; Ruban, A. V.; Skriver, H. L.; Kollár, J. The Surface Energy of Metals. *Surf. Sci.* **1998**, *411* (1), 186–202. [https://doi.org/10.1016/S0039-6028\(98\)00363-X](https://doi.org/10.1016/S0039-6028(98)00363-X).
- (36) Patra, A.; Bates, J. E.; Sun, J.; Perdew, J. P. Properties of Real Metallic Surfaces: Effects of Density Functional Semilocality and van Der Waals Nonlocality. *Proc. Natl. Acad. Sci.* **2017**, *114* (44), E9188–E9196. <https://doi.org/10.1073/pnas.1713320114>.
- (37) Singh-Miller, N. E.; Marzari, N. Surface Energies, Work Functions, and Surface Relaxations of Low-Index Metallic Surfaces from First Principles. *Phys. Rev. B* **2009**, *80* (23), 235407. <https://doi.org/10.1103/PhysRevB.80.235407>.
- (38) Da Silva, J. L. F.; Stampfl, C.; Scheffler, M. Converged Properties of Clean Metal Surfaces by All-Electron First-Principles Calculations. *Surf. Sci.* **2006**, *600* (3), 703–715. <https://doi.org/10.1016/j.susc.2005.12.008>.
- (39) Skriver, H. L.; Rosengaard, N. M. Surface Energy and Work Function of Elemental Metals. *Phys. Rev. B* **1992**, *46* (11), 7157–7168. <https://doi.org/10.1103/PhysRevB.46.7157>.
- (40) Tyson, W. R.; Miller, W. A. Surface Free Energies of Solid Metals: Estimation from Liquid Surface Tension Measurements. *Surf. Sci.* **1977**, *62* (1), 267–276. [https://doi.org/10.1016/0039-6028\(77\)90442-3](https://doi.org/10.1016/0039-6028(77)90442-3).
- (41) Boer, F. R. de; Mattens, W. C. M.; Boom, R.; Miedema, A. R.; Niessen, A. K. Cohesion in Metals. **1988**.
- (42) Xantheas, S. S. On the Importance of the Fragment Relaxation Energy Terms in the Estimation of the Basis Set Superposition Error Correction to the Intermolecular Interaction Energy. *J. Chem. Phys.* **1996**, *104* (21), 8821–8824. <https://doi.org/10.1063/1.471605>.
- (43) Hansen, M. H.; Torres, J. A. G.; Jennings, P. C.; Wang, Z.; Boes, J. R.; Mamun, O. G.; Bligaard, T. An Atomistic Machine Learning Package for Surface Science and Catalysis. *ArXiv190400904 Phys.* **2019**.
- (44) Henkelman, G.; Uberuaga, B. P.; Jónsson, H. A Climbing Image Nudged Elastic Band Method for Finding Saddle Points and Minimum Energy Paths. *J. Chem. Phys.* **2000**, *113* (22), 9901–9904. <https://doi.org/10.1063/1.1329672>.

- (45) Conrad, H.; Ertl, G.; Latta, E. E. Adsorption of Hydrogen on Palladium Single Crystal Surfaces. *Surf. Sci.* **1974**, *41* (2), 435–446. [https://doi.org/10.1016/0039-6028\(74\)90060-0](https://doi.org/10.1016/0039-6028(74)90060-0).
- (46) Herron, J. A.; Tonelli, S.; Mavrikakis, M. Atomic and Molecular Adsorption on Pd(111). *Surf. Sci.* **2012**, *606* (21), 1670–1679. <https://doi.org/10.1016/j.susc.2012.07.003>.
- (47) Fonseca, S.; Maia, G.; Pinto, L. M. C. Hydrogen Adsorption in the Presence of Coadsorbed CO on Pd(111). *Electrochem. Commun.* **2018**, *93*, 100–103. <https://doi.org/10.1016/j.elecom.2018.06.016>.
- (48) Atkins, P.; de Paula, J. *Physical Chemistry*, 10th ed.; Oxford University Press, 2014.
- (49) Tang, Q.; Shi, F.; Li, K.; Ji, W.; Leszczynski, J.; Russell, A. G.; Eddings, E. G.; Shen, Z.; Fan, M. Unveiling the Critical Role of P-d Hybridization Interaction in M13–nGan Clusters on CO₂ Adsorption. *Fuel* **2020**, *280*, 118446. <https://doi.org/10.1016/j.fuel.2020.118446>.
- (50) Brix, F.; Desbuis, V.; Piccolo, L.; Gaudry, É. Tuning Adsorption Energies and Reaction Pathways by Alloying: PdZn versus Pd for CO₂ Hydrogenation to Methanol. *J. Phys. Chem. Lett.* **2020**, *11* (18), 7672–7678. <https://doi.org/10.1021/acs.jpcllett.0c02011>.
- (51) Fujitani, T.; Saito, M.; Kanai, Y.; Watanabe, T.; Nakamura, J.; Uchijima, T. Development of an Active Ga₂O₃ Supported Palladium Catalyst for the Synthesis of Methanol from Carbon Dioxide and Hydrogen. *Appl. Catal. Gen.* **1995**, *125* (2), L199–L202. [https://doi.org/10.1016/0926-860X\(95\)00049-6](https://doi.org/10.1016/0926-860X(95)00049-6).
- (52) Haunschild, R.; Klopper, W. New Accurate Reference Energies for the G2/97 Test Set. *J. Chem. Phys.* **2012**, *136* (16), 164102. <https://doi.org/10.1063/1.4704796>.
- (53) Wellendorff, J.; Lundgaard, K. T.; Jacobsen, K. W.; Bligaard, T. MBEEF: An Accurate Semi-Local Bayesian Error Estimation Density Functional. *J. Chem. Phys.* **2014**, *140* (14), 144107. <https://doi.org/10.1063/1.4870397>.
- (54) Díez-Ramírez, J.; Valverde, J. L.; Sánchez, P.; Dorado, F. CO₂ Hydrogenation to Methanol at Atmospheric Pressure: Influence of the Preparation Method of Pd/ZnO Catalysts. *Catal. Lett.* **2016**, *146* (2), 373–382. <https://doi.org/10.1007/s10562-015-1627-z>.
- (55) Díez-Ramírez, J.; Díaz, J. A.; Sánchez, P.; Dorado, F. Optimization of the Pd/Cu Ratio in Pd-Cu-Zn/SiC Catalysts for the CO₂ Hydrogenation to Methanol at Atmospheric Pressure. *J. CO₂ Util.* **2017**, *22*, 71–80. <https://doi.org/10.1016/j.jcou.2017.09.012>.
- (56) Bahruji, H.; Bowker, M.; Jones, W.; Hayward, J.; Ruiz Esquiús, J.; Morgan, D. J.; Hutchings, G. J. PdZn Catalysts for CO₂ Hydrogenation to Methanol Using Chemical Vapour Impregnation (CVI). *Faraday Discuss.* **2017**, *197*, 309–324. <https://doi.org/10.1039/C6FD00189K>.